Int. J. Electrochem. Sci., 17 **(2022)** Article Number: 221137, doi: 10.20964/2022.11.38

International Journal of
ELECTROCHEMICAL
SCIENCE
www.electrochemsci.org

Short Communication

Investigation on Effect of Cathodic Protection and Imidazoline Inhibitor on Electrochemical Performance of 20MnSi Steel under Alternating Temperature Condition

Hao Chen[*], *Xue Pan*

Wuhan City Polytechnic, Hubei Wuhan, 430072, China
[*]E-mail: wu_chen0072@163.com

Received: 14 August 2022 / *Accepted:* 14 September 2022 / *Published:* 10 October 2022

The failure of reinforcements in rammed earth has been paid more attention to. However, under the alternating temperature conditions, the effect of cathodic protection and inhibitor on reinforcements was doubtful. In this paper, 20MnSi steel was adopted as the research object, and the micro morphology and electrochemical tests were carried out to determine the effect of cathodic protection and inhibitor. The results showed that the number of pits on the surface of 20MnSi steel after 50 cycles of temperature alternation decreased and the corrosion area increased under the cathodic proteticon and inhibitor. Moreover, with the increase of CP potential, the number of pits and the maximum pit depth decreased significantly. Further, the cathodic protection can provide the electrochemical protection, while the synergistic effect of cathodic protection and inhibitor presented a resistance-electrochemical protection. Under the alternating temperature condition, the phase evolution caused by carbonation of 20MnSi steel was the main failure reason. However, the corrosion protection provided by cathodic protection and imidazoline inhibitor for 20MnSi steel can only be achieved by inhibiting the electrochemical reaction process.

Keywords: Temperature alternation; 20MnSi steel; Cathodic protection; Imidazoline inhibitor; Electrochemical Performance

1. INTRODUCTION

The application of cathodic protection (CP) mainly started from 1973. During this period, researchers mainly devoted to the development of monitoring system and anode system corresponding to cathodic protection, and many scholars had made outstanding contributions [1,2]. Gadve et al. [3,4] applied impressed current cathodic protection (ICCP) to the corroded reinforcements. The auxiliary anode for cathodic protection was carbon fiber composite grid cloth (GFRP), and the applied current was 50 mA and 150 mA, respectively. The experimental results showed that the reinforcements inside the rammed earth can be well protected by GFRP as an auxiliary anode, and the mechanical properties

of the reinforced rammed earth specimens strengthened by GFRP were improved to a certain extent. Zhu et al. [5,6] used CFRP as the structural reinforcement agent and anode of the ICCP system, to study the mechanical and electrochemical properties of CFRP, and then explore the mechanism of improving the bearing capacity and durability of reinforced rammed earth structures. The results of potential tests showed that CFRP presented stable anodic performance in simulated pore solution. The tensile properties of CFRP decreased with the increase of CP current density. In conclusion, the application of the ICCP technology can effectively inhibit the corrosion of reinforcements in rammed earth, but only the application of the cathodic protection cannot improve the bearing capacity of the corroded reinforcements.

The advantages of corrosion inhibitor, such as small usage, low economic cost, remarkable use effect, and remedial to the damaged rammed earth structure, had attracted the attention of the majority of scholars. Corrosion inhibitors protected reinforcements by preventing cathodic or anodic reactions. The corrosion inhibition mechanism of corrosion inhibitors in rammed earth was mainly to promote the passivation of reinforcement surface or strengthen the passivation film formed, or to form adsorption or precipitation film on the surface of reinforcements. Nowadays, some more intelligent composite corrosion inhibitors protected the reinforcements through two slow-release mechanisms. At present, the corrosion inhibitors used in rammed earth system can be divided into inorganic corrosion inhibitors, organic corrosion inhibitors, blocking or barrier corrosion inhibitors and new green corrosion inhibitors. Wang et al. [7] studied the corrosion inhibition effect of sodium aluminate on galvanized reinforcements in simulated pore solution with or without chloride ions. The results showed that in the early stage of corrosion, the surface of reinforcements will quickly form a protective film containing Mo element, which prevented the rapid dissolution of zinc in the high alkaline environment and inhibited the hydrogen evolution reaction, so that the galvanized reinforcements and rammed earth maintained good bond performance. Mansour et al. [8] found that the addition of trisodium phosphate to the pore solution of simulated rammed earth containing chloride ions increased the ratio of Cl^- to OH^-. Zhang et al. [9] studied the corrosion inhibition effect of corn gluten extract on carbon steel in 3.0 wt.% NaCl solution, and the results showed that the phthalide bond in the extract would adsorb to the active part of the carbon steel, thus making the corrosion inhibition efficiency of carbon steel reached 88.10%. Liu et al. [10] showed that ginger extract can reduce the corrosion of reinforced rammed earth caused by Cl^- erosion, by inhibiting the anodic or cathodic reactions in the corrosion process by forming carbon-containing organic film. Zhao et al. [11] added the dodecyl benzene sulfonate triethanolamine salt to the pore solution of rammed earth, to reduce the pit corrosion on the reinforcements.

In previous studies, performance deterioration of reinforcements occurred under alternating temperature conditions [12]. Therefore, this paper comprehensively considered the combination of cathodic protection and imidazoline inhibitor to analyze the corrosion protection mechanism of reinforcements.

2. EXPERIMENT SETTINGS

The sample was made according to the method in paper [12], and the density of each specimen was 2.1-2.2×10^3 g/cm^3. 20MnSi steel was adopted as the research object, and its main components were shown in Table 1.

Table 1. The main component of 20MnSi steel (mass fraction, wt.%)

Element	C	Mn	Ni	Si	Cr	Fe
wt.%	0.19	1.43	0.028	0.49	0.026	Balance

The analytical pure reagent and deionized water were used to configure an experiment solution and the ionic composition was shown in Table 2 [12]. The water content of rammed earth was set to 5%, and the content of imidazoline inhibitor was 0.1 mol/L [13-23].

Table 2. The ionic composition of experiment solution

Component	$CaCl_2$	NaCl	Na_2SO_4	$MgSO_4·7H_2O$	KNO_3	$NaHCO_3$
Content /(g/L)	0.111	0.468	0.142	0.197	0.293	0.151

During the experiment, the prepared sample of 20MnSi steel with the size of 10×10×2 mm^3 was put into the experimental device as shown in Figure 1, and the experimental rammed earth was compacted through the cover plate to ensure the tightness and non-deformation of the experimental device [12]. The inner surface of the experimental device was made of iron, the outer surface was covered with an insulating layer, and the thermocouple was set in the middle to control the temperature. In this paper, the accelerated test method was adopted. The temperature range was set in 15-30℃, the heating/cooling rate was set at 1℃ / 10 min, and the 50 cycles were carried out [12].

The cathodic protection of 20MnSi steel under different alternating temperature cycles was applied by the DC source, in which the 20MnSi worked as the cathode and the Fe acted as the anode. The CP potential of -0.85~-1.2 V (vs. saturated calomel electrode, SCE) was impressed. When the 50^{th} temperature alternation was finished, the 20MnSi steel was taken out for the microscope morphology analysis and EIS (electrochemical impedance spectroscopy) test. It should be noted that in this paper, the condition for EIS test was in simulated solution according to Table 2 containing (no) imidazoline inhibitor under different CP potential. The frequency range of EIS tests was 10^{-2}-10^5 Hz, and the experiment temperature was set at 25℃.

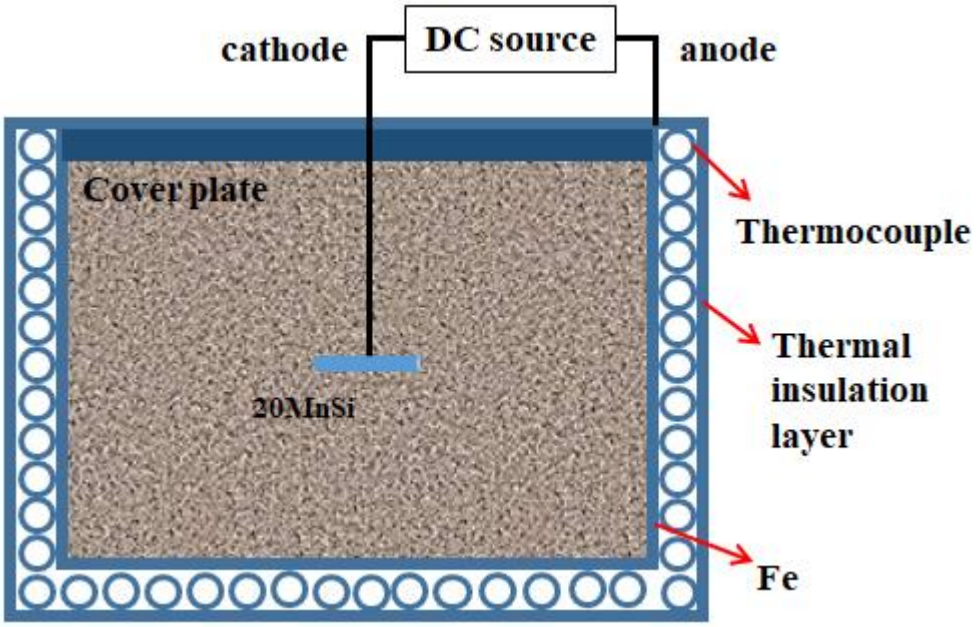

Figure 1. The experimental device for applying alternating temperature in different cycles on 20MnSi steel in rammed earth containing (no) imidazoline inhibitor under different CP potential of -0.85~-1.20 V (SCE)

3. RESULTS AND DISCUSSION

3.1 Microscope morphology

Figure 3 showed the microscope morphology and maximum pit depth of 20MnSi steel under different CP potentials and corrosion inhibitors. As can be seen from the figure, the surface of 20MnSi steel was densely covered with corrosion pits after 50 cycles of temperature alternation under no cathodic protection and inhibitor, and the maximum pit depth reached 71.369 μm, as shown in Figure 2(1a). When cathodic protection was applied, the number of pits decreased and the corrosion area increased at CP = -0.85 V (SCE), and the maximum pit depth increasely reached 104.679 μm, as shown in Figure 2(1b). With the increase of CP potential, the number of pits and the maximum pit depth decreased significantly. When the CP potential was -1.20 V (SCE), the maximum pit depth decreased to 26.944 μm, as shown in Figure 2(1f). When the corrosion inhibitor was added, the number of corrosion pits on the surface of 20MnSi steel decreased rapidly [24], but the area of corrosion pits increased significantly at CP = -0.85 V (SCE) [24,25], as shown in Figure 2(2b). Under this circumstance, the maximum pit depth was 88.365 μm, which was smaller than the maximum pit depth under cathodic protection alone [24-27]. As the CP potential continued to increase, the maximum pit depth of 20MnSi steel also decreased under the synergistic effect of cathodic protection and corrosion inhibitor. However, it can be seen from the figure that, under the study conditions in this paper, when the cathodic protection potential was -1.20 V (SCE) as shown in Figure 2(2f), the surface of 20MnSi steel still showed obvious roughness [28-30].

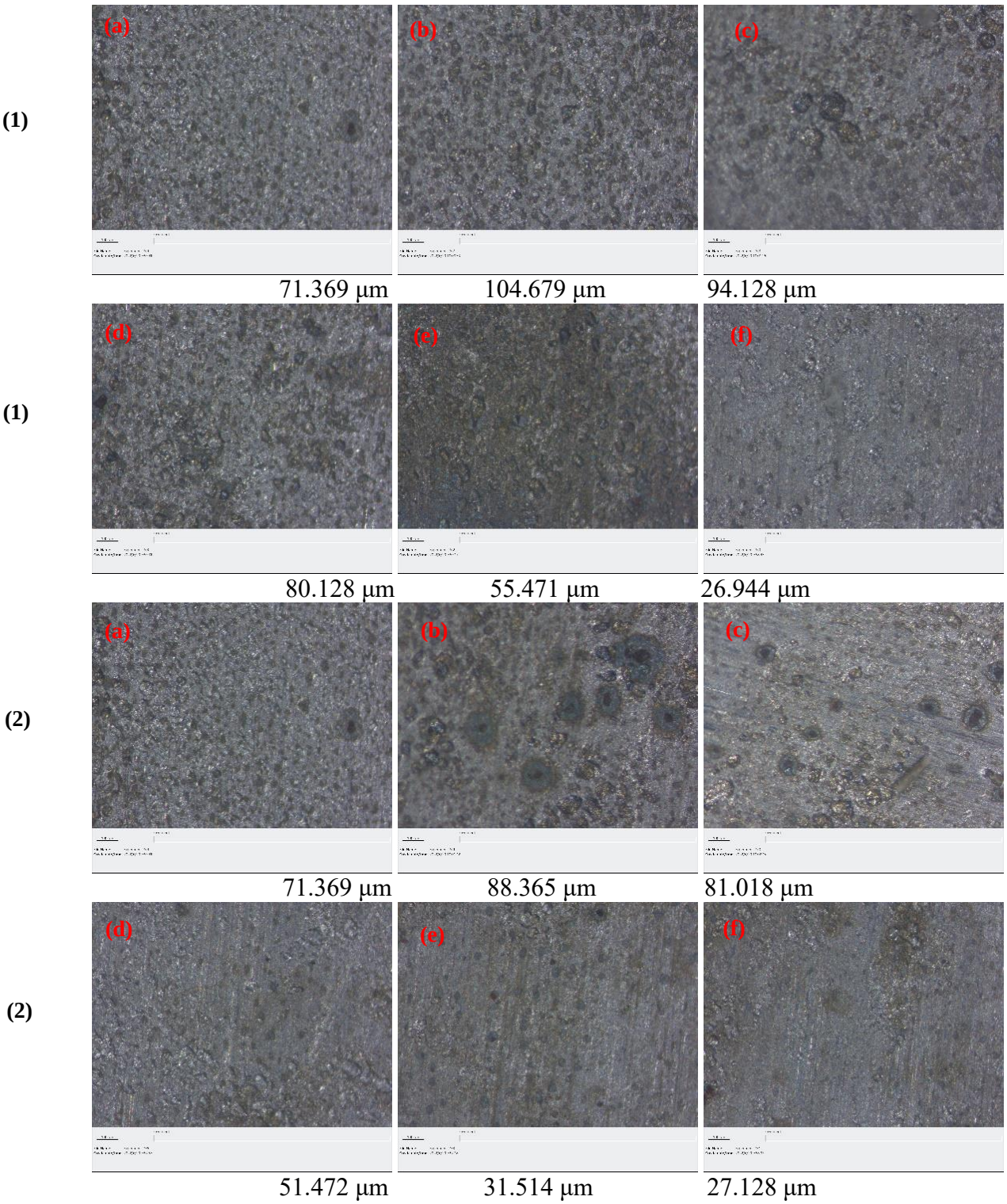

Figure 2. The microscope morphology (×200) and maximum pit depth of 20MnSi steel under the CP potential of -0.85~-1.20 V (SCE) (1) without or (2) with imidazoline inhibitor at 50th cycle of temperature alternation in the range of 15-30℃ with the rate of 1℃ / 10 min: (a) CP = 0, (b) CP = -0.85 V, (c) CP = -0.90 V, (d) CP = -1.00 V, (e) CP = -1.10 V, and (f) CP = -1.20 V

3.2 EIS curves

Figure 3 showed the EIS curves of 20MnSi steel under different CP potentials and corrosion inhibitors. The Nyquist diagram of 20MnSi steel showed incomplete capacitive arc at 50th cycle of temperature alternation under no cathodic protection and inhibitor. Under this circumstance, considering the electrochemical corrosion process, the equivalent electric circuit was chosen as $R_s(Q(R_p(C_{dl}R_{ct}))$, where R_s was the solution resistance, Q was the constant phase angle element, R_p was the surface resistance, C_{dl} was the double-layer capacitance, and R_{ct} was the charge-transfer resistance [31]. When cathodic protection was applied, under the condition of lower CP potential in -0.85~-1.00 V (SCE), the Warburg diffusion characteristic occurred in Nyquist diagram [32]. Meanwhile, in the log$f$-φ curve, the maximum phase angle (φ_{max}) appeared at the low-frequency position, which was represented by mass diffusion [32]. Therefore, the equivalent electric circuit was chosen as $R_s(QW(R_p(C_{dl}R_{ct}))$, where W was the Warburg diffusion resistance. With the sequentially increase of applied CP potential in -1.10~-1.20 V (SCE), the Nyquist diagram of 20MnSi steel showed a complete capacitive arc, and the maximum phase angle moved to the high frequency representing charge transfer, so the equivalent electric circuit was chosen as $R_s(Q(R_p(C_{dl}R_{ct}))$ [33-36]. However, there were impedance characteristics in Nyquist diagram when the imidazoline inhibitor was added. This was mainly because the surface state of 20MnSi steel was affected by CP potential and inhibitor [37-41], and further the cathodic protection an inhibitor showed the similar effect of reducing the corrosion. Therefore, the equivalent electric circuit was chosen as $R_s(QW(R_p(C_{dl}(R_{ct}L)))$, where L was the inductive reactance. Figure 4 showed the fitting results of relevant parameters under different conditions.

It can be seen from the previous research results in paper [12] that after 50th cycles were applied, the tensile strength of 20MnSi steel decreased from 410 MPa to 232.8 MPa, while the yield strength decreased from 245 MPa to 242.3 MPa, indicating that the mechanical properties of 20MnSi steel changed from plasticity to brittleness. Therefore, under no cathodic protection and inhibitor, on the one hand, CrO_3 formed by Cr precipitated on the surface of 20MnSi steel had a protective effect, so the capacitance (Q = 9.50×10^{-3} F/cm^2) and surface resistance (R_p = 34.63 Ω·cm^2) were relatively larger [42]. On the other hand, the precipitated second phase of the 20MnSi steel aggravated corrosion, so the double-layer capacitance (C_{dl} = 3.96×10^{-3} F/cm^2) and charge-transfer resistance were both smaller (R_{ct} = 22.66 Ω·cm^2) [43].

Since the surface of 20MnSi steel was covered with CrO_3 protective layer, when a lower CP potential of -0.85~-1.00 V (SCE) was applied, the depolarization process occurred to remove the CrO_3 protective layer, leading to the diffusion. Under this circumstance, the maximum phase angle frequency (f-φ_{max}) moved to the intermediate frequency from 0.85 Hz to 13.74 Hz, and the mass diffusion resistance ($|Z|$ at 10^{-2} Hz) decreased from 269.46 Ω to 160.27 Ω. When a larger CP potential of -1.10~-1.20 V (SCE) was applied, the 20MnSi steel was completely protected, in which the maximum phase angle slightly increased, i.e., φ_{max} = 58.76° at CP = -1.20 V (SCE), while the maximum phase angle frequency appeared in the high frequency region, i.e., f-φ_{max} = 2043.36 Hz at CP = -1.20 V (SCE), with an increasing mass diffusion impedance ($|Z|$ at 10^{-2} Hz = 669.53 Ω at CP = -1.20 V (SCE)), indicating that the charge-transfer process mainly occurred at this time [44]. However,

it should be noted that at this time, the capacitance (Q = 2.581×10^{-5} F/cm^2 and C_{dl} = 2.136×10^{-7} F/cm^2) and surface resistance (R_p = 19.2 Ω·cm^2) were all smaller, while the charge-transfer resistance (R_{ct} = 6804 Ω·cm^2) was bigger, which indicated that the structure of 20MnSi steel was destroyed and its corrosion resistance was lower due to the influence of temperature alternation [45-47]. The corrosion resistance mainly came from the inhibition of charge-transfer process under the cathodic protection.

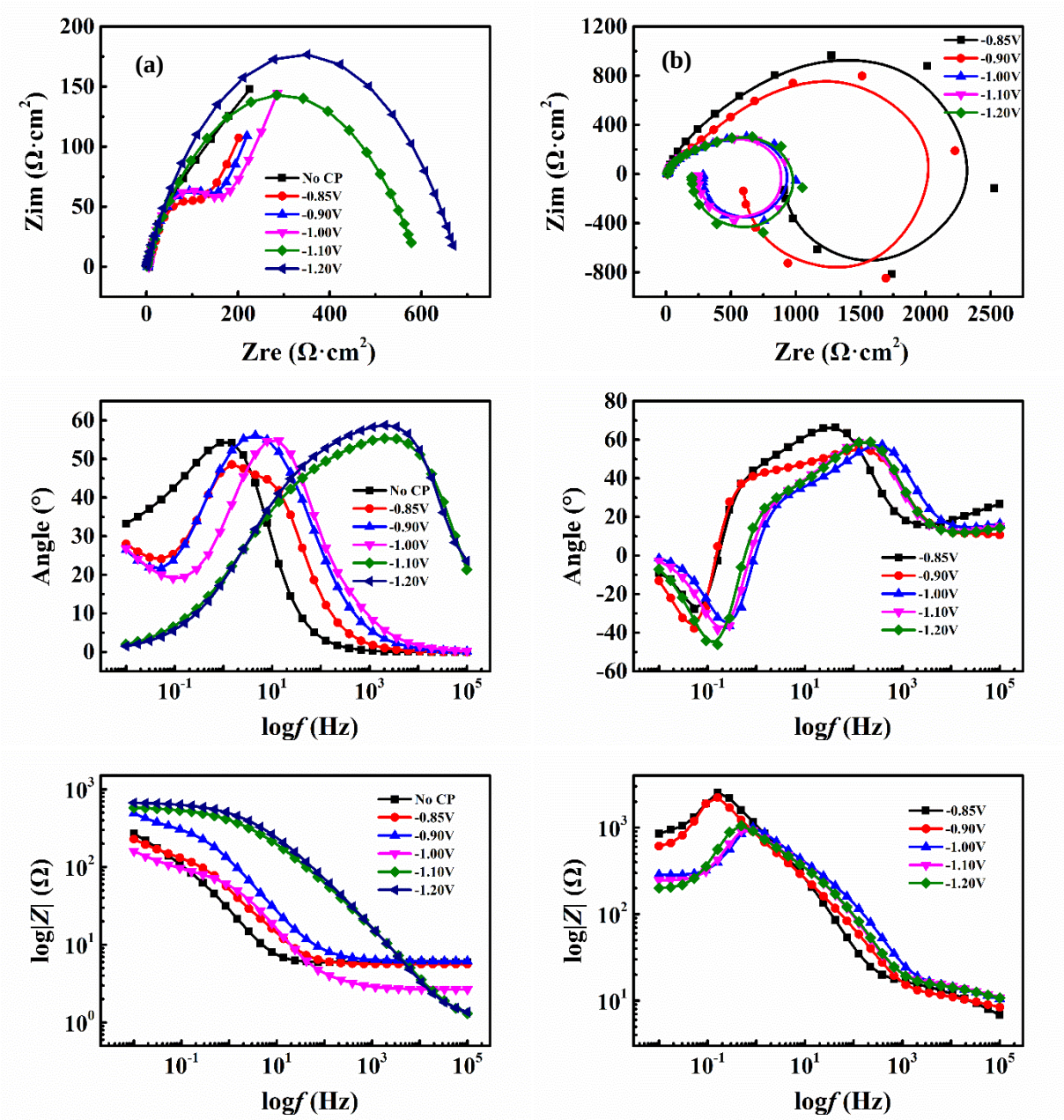

Figure 3. The comparison of EIS curves of 20MnSi steel under the CP potential of -0.85~-1.20 V (SCE) (a) with or (b) without imidazoline inhibitor at 50th cycle of temperature alternation in the range of 15-30℃ with the rate of 1℃ / 10 min in 3 wt.% NaCl solution at 25℃

When imidazoline inhibitor was added, with the increase of applied CP potential, the radius of Nyquist diagram including capacitive and induced arcs decreased, and the maximum phase angle

decreased slightly (φ_{max} = 66.38° at CP = -0.85 V (SCE)) and then remained unchanged (φ_{max} = 57.55° in CP = -0.90~-1.20 V (SCE)). The maximum phase angle frequency moved from medium frequency to high frequency (f-φ_{max} = 41.75 Hz → 385.66 Hz), and the mass diffusion resistance ($|Z|$ at 10^{-2} Hz) decreased from 850.00 Ω to 200.49 Ω. At this time, the capacitance (Q and C_{dl}) and resistance (R_p and R_{ct}) were at a small level, but the C_{dl} = 9.802×10^{-6} F/cm^2 under CP = -1.20 V (SCE) and inhibitor was larger than that (C_{dl} = 2.136×10^{-7} F/cm^2) under cathodic protection. Combined with the change of maximum phase angle frequency, the pure electrochemical protection was transformed into a resistance-electrochemical protection.

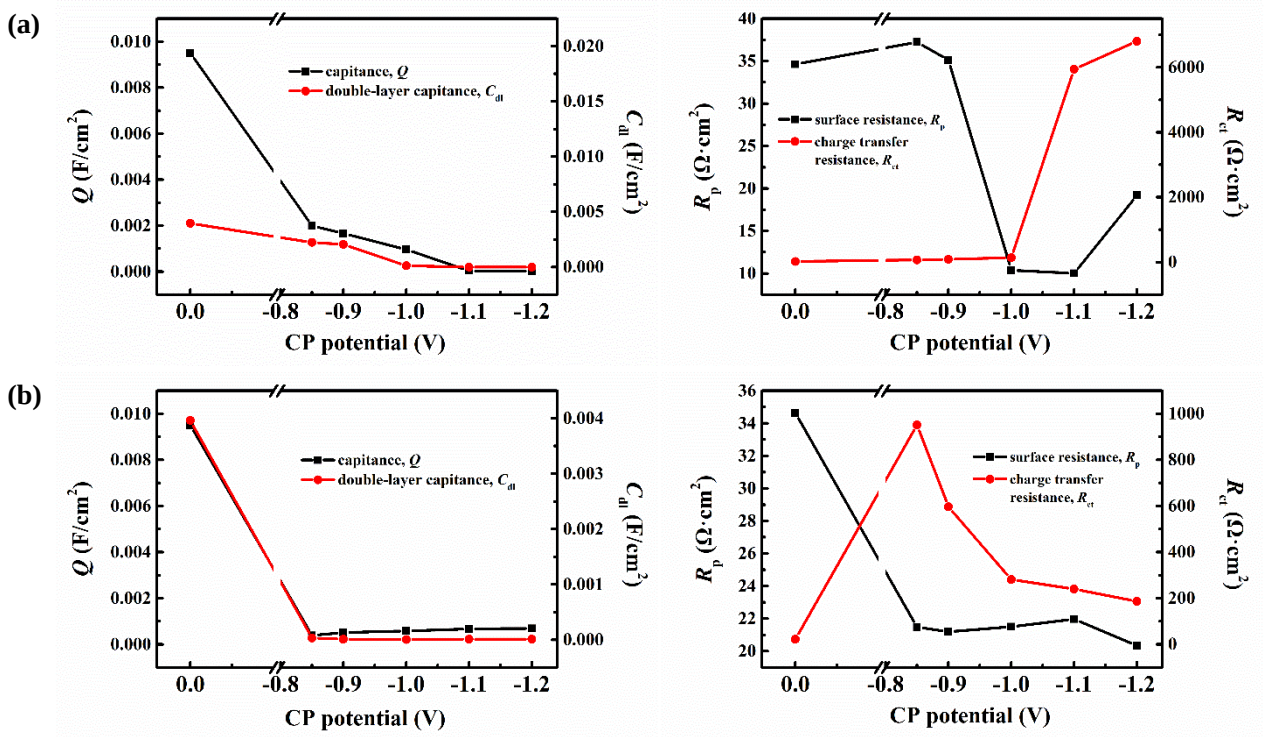

Figure 4. The fitting parameters including capacitance (Q), surface resistance (R_p), double-layer capacitance (C_{dl}) and charge transfer resistance (R_{ct}) of EIS curves of 20MnSi steel under the CP potential of -0.85~-1.20 V (SCE) (a) with or (b) without imidazoline inhibitor at 50th cycle of temperature alternation in the range of 15-30℃ with the rate of 1℃ / 10 min in 3 wt.% NaCl solution at 25℃

3.3 Effect of cathodic protection and imidazoline inhibitor on phase evolution of 20MnSi steel

In order to clarify the synergistic effect of cathodic protection and imidazoline inhibitor on 20MnSi steel under alternating temperature condition, Figure 5 showed the microscope morphology of 20MnSi steel after 50 cycles of temperature alternation. It can be seen from the figure that a large number of fine particles were still precipitated in 20MnSi steel and concentrated in the grain boundary of 20MnSi steel at CP = -1.20 V (SCE). After the imidazoline inhibitor was applied, the precipitated particles dispersed on the surface of 20MnSi steel and continued to distribute at the grain boundary. The precipitated fine particles gather and grow in grain boundaries, forming lumps or strips. However, what was initially a continuous network structure or skeleton structure became discontinuous.

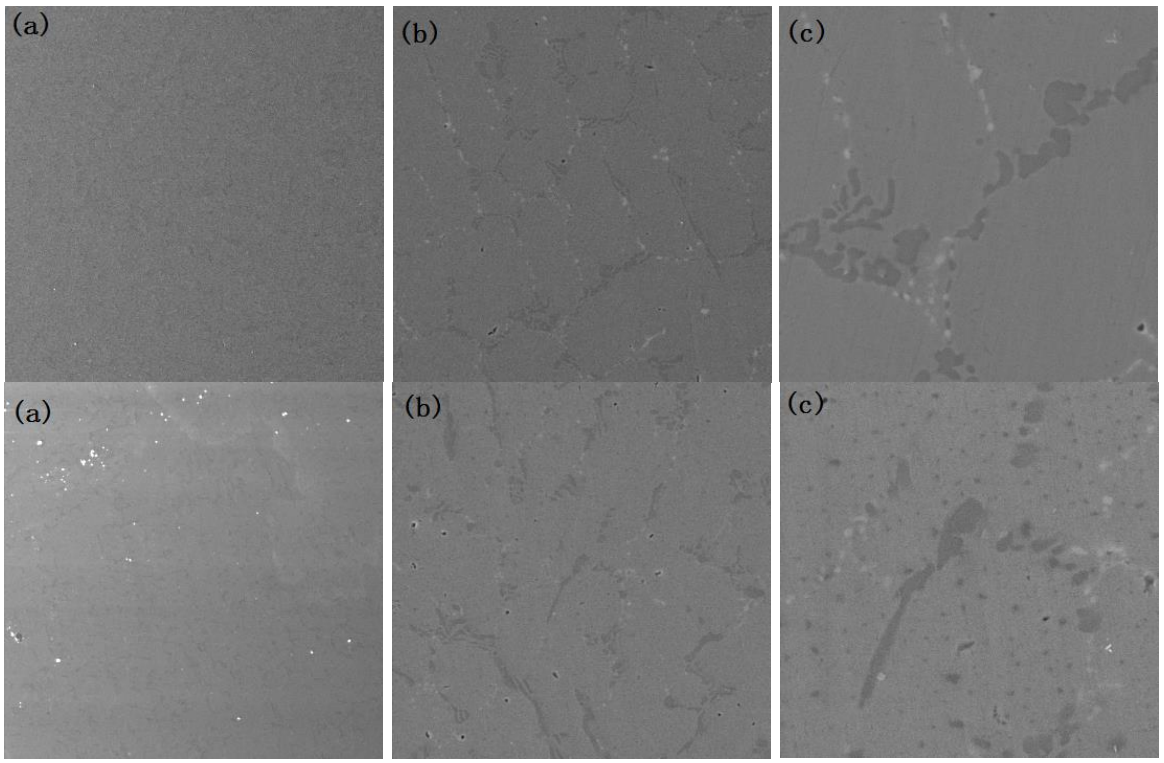

Figure 5. The microscopic morphology of 20MnSi steel at CP = -1.20 V (SCE) (1) with or (2) without imidazoline inhibitor at 50th cycle of temperature alternation in the range of 15-30℃ with the rate of 1℃ / 10 min: (a) ×200, (b) ×1000, and (c) ×3000

The EDS (Energy Dispersive Spectroscopy) scanning was carried out to analyze the chemical composition of 20MnSi steel after 50 cycles of temperature alternation under cathodic protection and inhibitor, as shown in Figure 6. The results showed that the precipitates were mainly composed of Fe, Cr, and Ni elements, which was consistent with the results in paper [12] under no cathodic protection and inhibitor.

The phase evolution of 20MnSi steel had its particularity during temperature alternation. When 50 cycles of temperature alternation were completed, a large number of dispersed secondary carbides of 20MnSi steel were produced, but under the cathodic protection and inhibitor, such secondary carbides will dissolve or merge in grain boundaries, resulting in a decrease of secondary carbides in surface [48,49]. The main reason was that the C content in 20MnSi steel was super-saturated, so The C was combined with alloy element to form the Cr-rich $M_{23}C_6$ carbides and then precipitated as dispersed secondary carbides. However, the fine carbide particles cannot be stable at high temperatures due to their small volume, and gradually dissolved and merged to lead a decreasing number of secondary carbides [50]. Accordingly, $M_{23}C_6$ carbides will grow coarsely. In conclusion, with the extension of service time, the precipitation amount of secondary carbides will reach a peak. However, in view of the above process, cathodic protection and imidazoline inhibitor were difficult to inhibit the evolution process of 20MnSi steel, and the corrosion protection of 20MnSi steel can only be achieved by inhibiting the surface electrochemical reaction process.

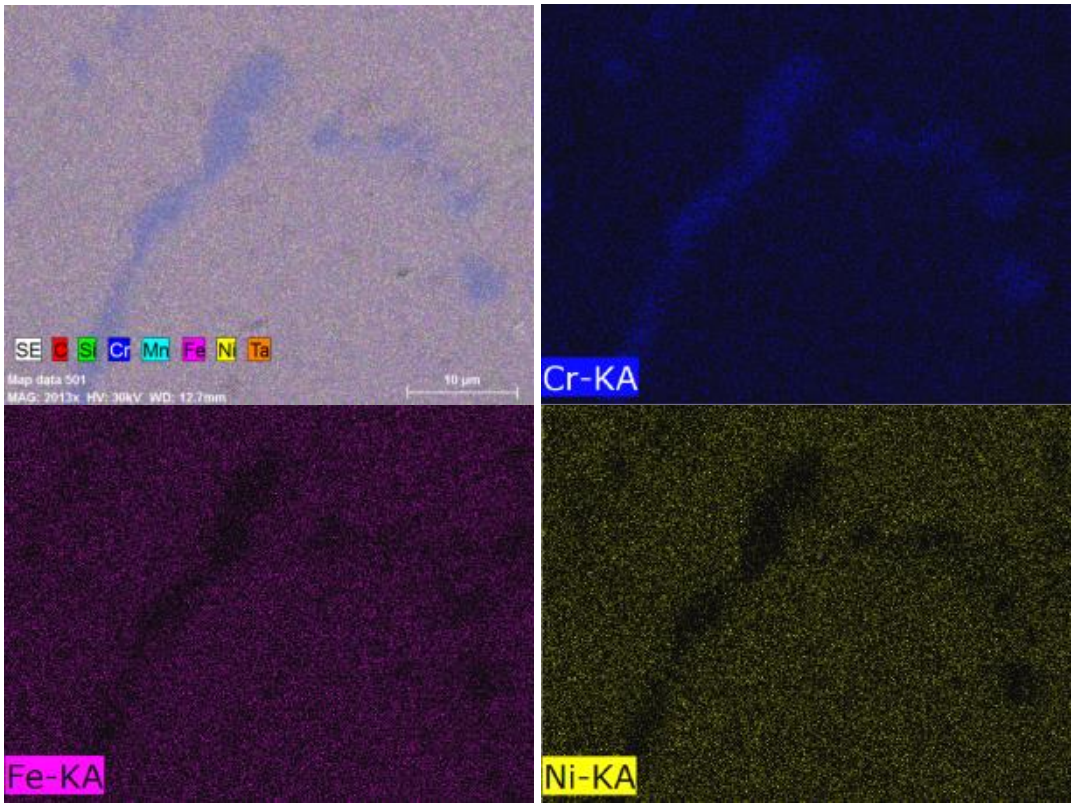

Figure 6. The EDS analysis of 20MnSi steel at CP = -1.20 V (SCE) with imidazoline inhibitor at 50th cycle of temperature alternation in the range of 15-30℃ with the rate of 1℃ / 10 min

4. CONCLUSIONS

In this paper, the effect of cathodic protection and inhibitor on 20MnSi steel under the alternating temperature conditions was studied by the micro morphology and electrochemical tests. The following conclusions were drawn.

(1) The surface of 20MnSi steel was densely covered with corrosion pits after 50 cycles of temperature alternation under no cathodic protection and inhibitor. When cathodic protection and inhibitor were applied, the number of pits decreased and the corrosion area increased, and with the increase of CP potential, the number of pits and the maximum pit depth decreased significantly.

(2) When a lower CP potential of -0.85~-1.00 V (SCE) was applied, the depolarization process occurred to remove the CrO_3 protective layer, leading to the diffusion. The corrosion resistance mainly came from the inhibition of charge-transfer process under the increasing CP potential in -1.10~-1.20 V (SCE). When corrosion inhibitor was added, the Nyquist diagrams showed the inductive characteristics, and the double-layer capacitance increased, while the maximum phase angle frequency appeared at the intermediate frequency, indicating that the pure electrochemical protection was transformed into a resistance-electrochemical protection at this time.

(3) The phase evolution caused by carbonation of 20MnSi steel during temperature alternation was the main failure reason. However, the corrosion protection from cathodic protection and inhibitor of 20MnSi steel can only be achieved by inhibiting the surface electrochemical reaction process.

ACKNOWLEDGEMENTS
This study is supported by the Wuhan City Polytechnic project (2021whcvcC1) and Wuhan Education Bureau project (CXY201814).

Reference

1. C. Chen, L. Jiang, M.Z. Guo, P. Xu, L. Chen and J. Zha. *Constr. Build. Mater.*, 228 (2019) 116752.
2. J. Hu, Y. Zhu, J. Hang, Z. Zhang and J. Wei. *Constr. Build. Mater.*, 267 (2021) 121011.
3. S. Gadve, A. Mukherjee and S.N. Malhotra. *ACI Mater. J.*, 107 (2010) 349.
4. S. Gadve, A. Mukherjee and S.N. Malhotra. *Corrosion*, 67 (2011) 1.
5. J.H. Zhu, G. Guo, L. Wei, M. Zhu and X. Chen. *Materials,* 9 (2016) 103.
6. J H Zhu, M.C. Zhu, N.X. Han, W. Liu and F. Xing. *Materials,* 7 (2014) 5438.
7. Y.Q. Wang, G. Kong, C.S. Che and B. Zhang. *Constr. Build. Mater.*, 162 (2018) 383.
8. H.B. Mansour, L. Dhouibi and H. Idrissi. *Constr. Build. Mater.*, 171 (2018) 250.
9. Z. Zhang, H. Ba and Z. Wu. *Constr. Build. Mater.*, 227 (2019) 117080.
10. Y. Liu, Z. Song, W. Wang, L. Jiang, Y. Zhang, M. Guo, F. Song and N. Xu. *J. Clean. Prod.*, 214 (2019) 298.
11. Y. Zhao, T. Pan, X. Yu and D. Chen. *Corros. Sci.*, 158 (2019) 108097.
12. H. Chen and X. Pan. *Int. J. Electrochem. Sci.*, 17 (2022) 220728.
13. C. Googan. *Mater. Corros.*, 72 (2021) 446.
14. J. Nezgoda, G.B. Leoni and S.L.D.C. Brasil. *Chem. Eng. Technol.*, 44 (2021) 1094.
15. H. Xu, X.T. Wang, J.M. Niu, Y.B. Nan, J.Y. Pu, H. Zhou, J.Z. Duan, Y.L. Huang and B.R. Hou. *Adv. Mater. Interfaces*, 9 (2022) 2102085.
16. N. Al-Akhras and Y. Mashaqbeh. *J. Build. Eng.*, 35 (2021) 101848.
17. Q.Y. Liu, Z.J. Song, H. Han, S. Donkor, L.H. Jiang, W.Y. Wang and H.Q. Chu. *Constr. Build. Mater.*, 260 (2020) 119695.
18. A. Zomorodian, R. Bagonyi and A. Al-Tabbaa. *J. Build. Eng.*, 38 (2021) 102171.
19. Y. Zhang, Q.Q. Xu, M. Sun, C.S. Xiong, P. Wang, Z. Chen, G.X. Sun, J. Guan, Z.H. Ding, M.M. Li and D.S. Hou. *Constr. Build. Mater.*, 294 (2021) 123571.
20. F.L. Fei, J. Hu, J.X. Wei, Q.J. Yu and Z.S. Chen. *Constr. Build. Mater.*, 70 (2014) 43.
21. C.S. Sobhy, T.A. Tawfik, G.M.A. El Hafez and A.S. Faried. *Case Stud. Constr. Mat.*, 16 (2022) e01017.
22. X.Y. Yang, S.P. Fu, Q. Wang, Q.H. Sun, J.W. Zhang, Y.C. Peng, Z.Z. Liang and J.F. Li. *J. Mol. Struct.*, 1270 (2022) 133898.
23. L. Yohai and M. Vázquez and M.B. Valcarce. *Electrochim. Acta*, 102 (2013) 88.
24. G.X. He, H. Peng, K.X. Liao, M.N. Wang, S. Zhao and J.H. Leng. *Mater. Corros.*, 72 (2021) 839.
25. H.B. Xu, L. Li, Y. Zhao, H.Y. San, T. Zhang, X.D. Su and F.H. Wang. *Mater. Corros.*, 72 (2021) 720.
26. S. Mameri, D. Boughrara, F. Lazar and J. Chopart. *Steel Res. Int.*, 93 (2022) 2200050.
27. D.X. Liu, X.L. Qiu, M.L. Shao, J.C. Gao, J.J. Xu, Q.X. Liu, H. Zhou and Z.Z. Wang. *Mater. Corros.*, 70 (2019) 1907.
28. L. de S. Miranda, M. Nele and J.C. Pinto. *Macromol. React. Eng.*, 13 (2019) 1900027.
29. I. N. Shabanova, F. F. Chausov, E. A. Naimushina and N. V. Somov. *Surf. Interface Anal.*, 46 (2014) 750.
30. V. Srivastava, D.S. Chauhan, P.G. Joshi, V. Maruthapandian, A.A. Sorour and M.A. Quraishi. *ChemistrySelect*, 3 (2018) 1990.
31. D. Doležal, T. Bolanca and Š. C. Stefanović. *Materialwiss. Werkst.*, 42 (2011) 229.
32. R. Galvan-Martinez, R. Orozco-Cruz, R. Torres-Sanchez and E. A. Martinez. *Mater. Corros.*, 61

(2010) 872.
33. J. Du, S. Jia, F. Yang, Z.M. Wei, H.P. Song, X.D. Yang and F.S. Wang. *J. Surfactants Deterg.*, 22 (2019) 833.
34. B. Warren, G.J. Hunt, M. Bryant, A. Neville, A. Morina and M. Gahagan. *Lubr. Sci.*, 30 (2018) 301.
35. N.A. Odewunmi, M.A. J. Mazumder and S.A. Ali. *ChemistrySelect*, 6 (2021) 3199.
36. G.I. Ramírez-Peralta, U. León-Silva, M.E.N. Díaz and M.G. Valladares-Cisneros. *Mater. Corros.*, 69 (2018) 1631.
37. V. Saraswat and M. Yadav. *ChemistrySelect*, 5 (2020) 7347.
38. K. Kousar, T. Ljungdahl, A. Wetzel, M. Dowhyj, H. Oskarsson, A.S. Walton, M.S. Walczak and R. Lindsay. *J. Surfactants Deterg.*, 23 (2020) 225.
39. C. Gao, X. Zhao, K.Y. Liu, X.Y. Dong, S.J. Wang and F.G. Kong. *Mater. Corros.*, 71 (2020) 1903.
40. M. Fedel, M. Poelman, M. Olivier and F. Deflorian. *Surf. Interface Anal.*, 51 (2019) 541.
41. J. Roscher, D. Liu and R. Holze. *Mater. Corros.*, 73 (2022) 254.
42. S. Xiong, H. Wu, Z.Y. Liu, Y.C. Wang and W. Lin. *Mater. Corros.*, 53 (2021) 418.
43. M. Harilal, S. Uthaman, R.P. George, B. Anandkumar, C. Thinaharan, J. Philip and U.K. Mudali. *Environ. Prog. Sustain.*, 38 (2019) 13102.
44. A.A. Aghzzaf, D. Veys-Renaux and E. Rocca. *Mater. Corros.*, 71 (2020) 148.
45. A.E.E. Fouda, A.E.M. Ahmed, S.M. El-Darier and S.E. Badr. *J. Chin. Chem. Soc.*, 68 (2021) 1445.
46. D.G. Ladha, N.K. Shah, Z. Ghelichkhah, I.B. Obot, F.K. Dehkharghani, J.Z. Yao and D.D. Macdonald. *Mater. Corros.*, 69 (2018) 125.
47. C.M. Fernandes, M.V.P. de Mello, N.E. dos Santos, A.M.T. de Souza, M. Lanznaster and E.A. Ponzio. *Mater. Corros.*, 71 (2020) 280.
48. M.P. Petkov, M. Chevalier, D. Dean and A.C.F Cocks. *Int. J. Pres. Ves. Pip.*, 194 (2021) 104500.
49. W. Li, H.T. Chen, W.Y. Huang, J. Chen, C. Li, D. Xu, S. An, S. Zhang and H. Yang. *Eng. Fail. Anal.*, 128 (2021) 105611.
50. M.K. Jiang, Y. Han, J.Q. Sun, J. Sun, G. Zu, H. Chen and X. Ran. *Mater. Charact.*, 179 (2021) 111346.